Electrostatic Boundary Conditions and (Electro)chemical Interface Stability

ADVANCED MATERIALS INTERFACES
Open Access
www.advmatinterfaces.de

Electrostatic Boundary Conditions and (Electro)chemical Interface Stability

*Binxiang Huang, Paul Erhart, Tongqing Yang, and Andreas Klein**

Interface stability is a key factor for stable operation of electronic and electrochemical devices. This contribution introduces an approach for the operando analysis of interfaces using photoelectron spectroscopy employing a solid oxide electrochemical cell. The combined chemical and electronic information provided by the experiment reveals that not only chemical but also electrostatic boundary conditions are essential for interface stability. The approach is demonstrated using (anti-)ferroelectric (Pb,La)(Zr,Sn,Ti)O_3 dielectrics.

1. Introduction

Electrode interfaces are indispensable ingredients of electronic and electrochemical devices. Their stability under operating conditions is crucial for countless applications including, e.g., batteries, non-volatile memories, memristors, piezoelectric transducers, and capacitors.[1–5] The thermodynamic stability of materials is known to be restricted to a fixed range of chemical potentials (activities) of its constituents.[6] For example, an oxide is only stable if the oxygen chemical potential, which is connected to the oxygen partial pressure, is higher than the formation enthalpy of an oxide. In addition to the chemical potential of the (atomic) constituents, also the electron chemical potential, which via the charge neutrality condition determines the Fermi energy in a material, must also remain within a certain range. A related electrochemical instability can be induced in two ways: i) by the formation of self-compensating defects;[7] ii) by valence changes of the constituting elements.[8] Both phenomena are intimately connected to the dependence of the formation enthalpies of the defects involved on the electron chemical potential (**Figure 1**). In the case of self-compensation, the related defects are lattice point defects, such as vacancies or interstitials. With increasing electron chemical potential, the formation enthalpy of acceptor defects, such as cation vacancies, decreases, while for low electron chemical potentials, the formation enthalpy of donor defects, such as anion vacancies or cation interstitials, is reduced. Regarding valence changes, a high/low electron chemical potential favors a reduction/oxidation of lattice species. For both self-compensation and valence changes, the material is only stable thermodynamically when defect concentrations are low enough. This requires that the formation enthalpies of all defects are positive. Consequently, the material is only stable as long as its Fermi energy remains within the ranges indicated in Figure 1a. The electrochemical stability becomes particularly relevant at electrode interfaces, where the choice of electrode material determines the Fermi energy at the interface by its Schottky barrier height, which determines the electrostatic boundary condition independent of the chemical potentials.

Due to the importance of the electrostatic boundary condition, it is indispensable to probe both chemical and electronic properties of interfaces in order to reveal not only the conditions but also the origin of potential instabilities. X-ray photoelectron spectroscopy (XPS) is uniquely suited for this purpose as it provides exactly this combination of information. Ideally, interface stability should be analyzed under realistic or accelerated test conditions. The application of the technique will be demonstrated for undoped and La-doped Pb(Zr,Sn,Ti)O_3 (P(L)ZST). The La-doped sample exhibits an antiferroelectric polarization hysteresis loop, which is characterized by a reversible field-driven transition between an antipolar and a polar phase.[9] A characteristic hysteresis loop of an antiferroelectric capacitor is illustrated in Figure 1b. The green filled area corresponds to the recoverable energy density of the capacitor. Due to the specific shape of the hysteresis loop, antiferroelectric materials allow for the highest energy densities of inorganic dielectric capacitors, which are beneficial for their application in electric power conversion, for example in electric vehicles or renewable power generation systems.

Changing the electrostatic boundary condition at an interface becomes possible if an electrochemical cell is installed inside the XPS system with a top electrode being thin enough to allow photoelectrons from the interface to penetrate through the

B. Huang, A. Klein
Institute of Materials Science
Technical University of Darmstadt
Otto-Berndt-Str. 3, 64287 Darmstadt, Germany
E-mail: Andreas.Klein@tu-darmstadt.de
P. Erhart
Department of Physics
Chalmers University of Technology
SE-412, Gothenburg 96, Sweden
T. Yang
Functional Materials Research Laboratory
Tongji University
Cao'an Road 4800, Shanghai 201804, China
The ORCID identification number(s) for the author(s) of this article can be found under https://doi.org/10.1002/admi.202300332

DOI: 10.1002/admi.202300332

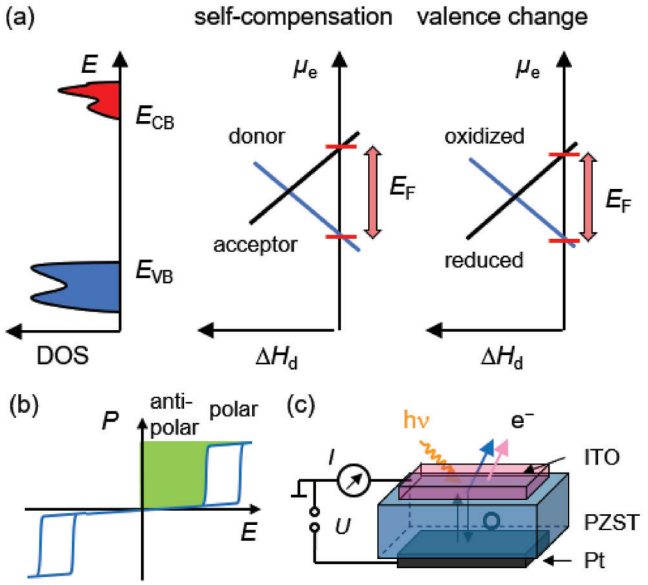

Figure 1. a) Schematic electronic band structure of a dielectric and the Fermi level limitation induced by self-compensation and valence change, which are caused by the dependence of the formation enthalpies, ΔH_d, of intrinsic donor and acceptor defects or of reduced and oxidized lattice species on the electron chemical potential, μ_e; The dielectric is only stable if the Fermi energy stays within the range of positive defect formation enthalpies; b) schematic polarization-field hysteresis loop of an antiferroelectric dielectric. The green area represents the recoverable energy density, which increases with polarization and with the electric field of the transition between the antipolar and the polar phase; c) configuration of the electrochemical cell used for XPS measurements of undoped and La-doped Pb(Zr,Sn,Ti)O_3 (P(L)ZST).

electrode. The corresponding configuration is depicted in Figure 1c. Operando XPS studies of electrochemical cells have been reported by other groups.[10–14] In these cases, different conducting oxides have been deposited onto Yttria-stabilized Zirconia (YSZ) single crystals. The YSZ serves as the electrolyte in these solid oxide cells and enables to change the oxygen content in the deposited material, the electrode of the cell. The present work extends this approach to study the interface stability of the electrolyte material. A key ingredient of the experiment is the top electrode, in which the Fermi energy can be controlled via the applied field. The conductivity of the electrode must also be high enough for proper operation of the cell at an electrode thickness of only a few nanometers. It will be shown that Sn-doped In_2O_3 (ITO) is well suited for this purpose.

P(L)ZST is a classical dielectric material that exhibits capacitor behavior in electrode/dielectric/electrode stacks. One of the issues with capacitors employing perovskite oxide dielectrics is resistance degradation. Applying sufficiently high direct current (dc) voltages, the leakage resistance increases with time and may eventually lead to dielectric breakdown, limiting the application at elevated temperatures.[15,16] Resistance degradation is typically measured in so-called highly accelerated lifetime tests (HALT), where the dc leakage current is measured versus time at elevated temperature. The increase of current can be quantitatively described by the ionic demixing model,[17] which is based on the field-induced oxygen migration and the induced changes of local electrical conductivity in dependence on oxygen vacancy concentration. Perovskite oxide dielectrics can thus also be considered as, albeit poor, ionic conductors. As ion migration is fundamental to the observation of interface instability in the presented experiments, we refer to the studied electrode/P(L)ZST/electrode stacks as "electrochemical cells" and not as capacitors.

2. Results and Discussion

Panels a,b of **Figure 2** display X-ray photoelectron survey spectra of the samples after heating to 250 °C. Emissions related to the ITO electrode layer are dominating the spectra. Only the Pb 4*f* emission from the P(L)ZST substrate is clearly visible. Graphs c–j display Pb 4*f*, Zr 3*d*, In 3*d*, and Sn 3*d* emissions recorded at room temperature, at 250 °C before application of electric fields, at 250 °C during the last measurement with an applied electric field, and without electric field after cooling down to room temperature. Before applying an electric field, the Pb 4*f* emission exhibits a single doublet structure, corresponding to Pb^{2+} in the P(L)ZST. In contrast to the case of $BiFeO_3$,[18] deposition of ITO onto P(L)ZST does not directly lead to a reduction of the substrate. At the end of the measurement sequence with increasing electric field, both samples exhibit two Pb 4*f* doublets, which are related to the perovskite phase and, at lower binding energy, to metallic Pb. Evidently, the samples are reduced at the interface upon cathodic polarization of the ITO electrode. The Zr 3*d* spectra exhibit binding energy shifts in parallel to those of the oxidic Pb 4*f* emissions. No changes of the peak shapes are observed. Ti 2*p* emissions from the P(L)ZST sample are too strongly attenuated by the ITO layer and could not be recorded.

The In 3*d* and Sn 3*d* spectra exhibit the same binding energy shifts with increasing electric field as the oxide component of the Pb 4*f* emission. An increasing binding energy of In and Sn indicates an increasing Fermi energy, corresponding to an increasing electron concentration. The asymmetries of the In 3*d* and Sn 3*d* spectra also increase with applied electric field. This further confirms that the increase of the binding energy is related to an increase of the Fermi energy in the ITO layer.[19] It is clear though that the ITO electrode layer remains intact during the measurement, as no metallic In or Sn species are observed. In panels d,f of Figure 2, a shift of the Pb 4*f* and the Zr 3*d* peaks of the PLZST sample to lower binding energies by 200–300 meV can be noticed upon heating of the sample. Such shifts are reproducibly observed upon heating in related experiments. They are likely assigned to changes of the energy gap that are of the same magnitude (for In_2O_3, please refer to [20]). Correspondingly, the peaks shift back to higher binding energy after cooling. The shifts are not evident for the PZST sample. This can be understood by other effects contributing the binding energy. The ITO layer can change its carrier concentration by exchange of oxygen with the substrate. This effect should be more pronounced for PZST, which exhibits a higher concentration of oxygen vacancies than the donor-doped P(L)ZST (see below). The spectra recorded from PZST at higher fields are also affected by charging effects (see below).

Panels a,b of **Figure 3** depict the evolution of the Pb 4*f* emission during application of an electric field at 250 °C. The appearance of metallic Pb is evident for both samples. For the highest fields, a gradual shift to higher binding energies is observed for

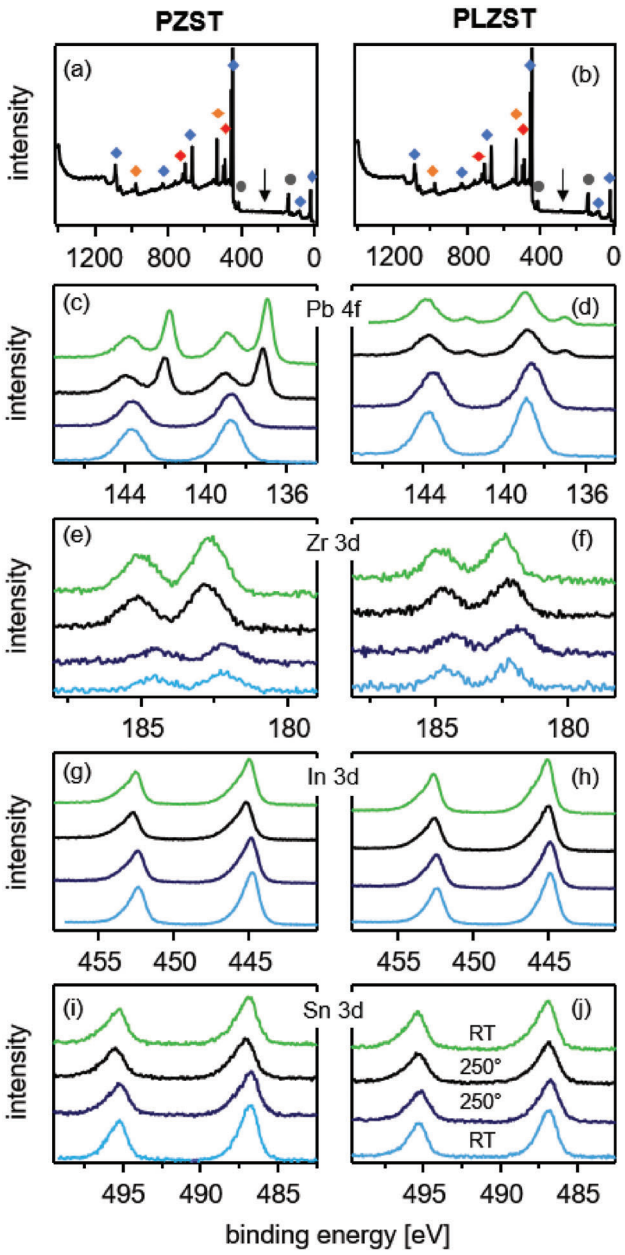

Figure 2. X-ray photoelectron spectra of PZST (left) and PLZST (right). Survey spectra after heating to 250 °C are shown in (a) and (b). Blue, red, and orange diamonds indicate emissions from In, Sn, and O, while grey circles and the arrows indicate the Pb 4*f* and C 1s peaks, respectively. The detail spectra (c–j) were recorded at room temperature (light blue), at 250 °C before application of an electric field (dark blue) and during the last measurement with applied electric fields (black), as well as after cooling down to room temperature and removal of the electric field (green).

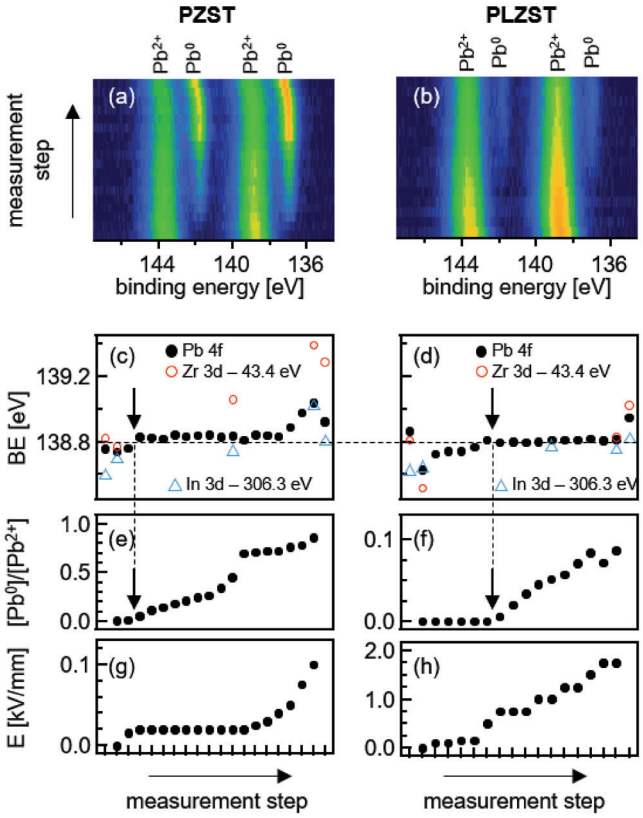

Figure 3. Color intensity maps of the Pb 4*f* spectra of nominally undoped a) and La-doped b) PZST recorded with applied fields at 250 °C. Panels c,d) show binding energies, while panels e,f) give the ratio of the metallic to the oxidic Pb component. The applied electric fields are shown in g,h). The arrows in (c)-(f) indicate the appearance of metallic Pb, which coincides with a Pb 4*f* binding energy of 138.8 eV. Note the different axis scaling of the electric fields and intensity ratios for PZST and PLZST.

the undoped PZST sample. As the metallic Pb and the In emissions exhibit the same shift, this shift can be associated to a voltage drop in the very thin ITO layer, related to the higher current flowing through the undoped PZST sample (see Supporting Information).

The observed reduction of Pb underneath the cathode electrode contrasts with the reduction of Ti, which has been reported in post-mortem analysis by means of transmission electron microscopy of the cathode interface after resistance degradation of $Pb(Zr,Ti)O_3$ (PZT) thin films.[21] The difference in reduction behavior can be assigned to the different compositions of the studied samples. The PZT thin film samples studied in Ref. [21] have a Zr/Ti ratio close to the morphotropic phase boundary and therefore contain a higher Ti fraction (48%) on the *B*-site of the perovskite lattice than the samples studied here (75% Zr). From a chemical point of view, a reduction of Ti to Ti^{3+} in Ti-rich PZT is favorable against a reduction of Pb, as the sum of formation enthalpies of Ti_2O_3 and PbO is lower than that of TiO_2 and Pb.[22] For pure $PbZrO_3$, a reduction of Zr is not possible as Zr-suboxides are not stable.[22] A preference for the chemical reduction of Pb against that of the *B*-site cations is therefore expected for more Zr-rich compositions.

The amount of metallic Pb is considerably higher for the undoped sample. This concurs with the expected higher concentration of oxygen vacancies in this sample. For the La-doped sample, a considerably lower concentration of oxygen vacancies is expected as common for donor-doped oxides.[23] Nevertheless, there must still be a sufficient concentration of oxygen vacancies in the PLZST in order to induce the reduction. The observed formation of metallic Pb is not necessarily induced by a high

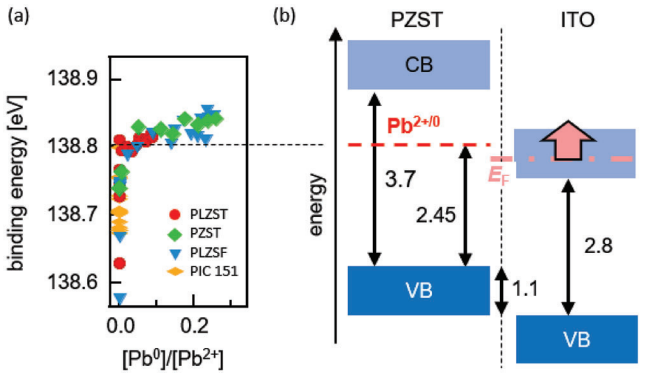

Figure 4. a) Binding energy of the Pb 4*f* emission versus Pb^0/Pb^{2+} intensity ratio and its relation to the energy band diagram of the top electrode interface. In addition to the P(L)ZST samples, results from a La-Fe codoped $Pb(Zr,Sn)O_3$ sample (PLZSF) and a commercial $Pb(Zr,Ti)O_3$ ferroelectric sample (PIC 151) are included in the plot; b) After deposition of ITO, the Fermi energy is below the reduction potential of Pb. Cathodic polarization raises the Fermi energy in ITO. The energy band alignment between P(L)ZST and ITO is derived from the binding energy differences between the Pb 4*f* and In 3*d* levels. It is the same for the doped and the undoped sample (see Figure 3c,d) and identical to the value reported for the PZT/ITO interface in [24].

concentration of oxygen vacancies, however. It may also be caused by a change of the Fermi energy and a consequent electrochemical reduction. The change of the Fermi energy at the interface is evident from the binding energy shifts, which are displayed in panels c,d of Figure 3. With increasing electric field, all binding energies increase, indicating an upward shift of the Fermi energy.

The amounts of metallic Pb for the two samples are given in panels e,f of Figure 3. As indicated by the arrows, the metallic Pb appears in both samples when the binding energy of the Pb^{2+}-component reaches 138.8 ± 0.05 eV. The correlation between the Pb 4*f* binding energy and the metallic Pb content is further emphasized in **Figure 4**a for four different samples, including those illustrated in Figures 2 and 3, a 2 % La - 2 % Fe codoped $Pb(Zr_{0.75}Sn_{0.25})O_3$ sample (PLZSF), and a commercial PZT ceramic with a Zr/Ti ratio near the morphotropic phase boundary (PIC 151 from PI ceramic, Lederhose, Germany). The latter does neither show metallic Pb nor does the binding energy of the Pb 4*f* peak reach 138.8 eV.

The correlation between the appearance of metallic Pb and the binding energy might be coincidental. However, the two observations do not have the same origin. In general, the Fermi energy at an insulator/metal contact is determined by the material with the higher density of states at the Fermi energy, ITO in the present case. An upward shift of the Fermi energy at the P(L)ZST/ITO interface must therefore be caused by an upward shift of the Fermi energy in the ITO layer as indicated in Figure 4b by the pink arrow. This change is induced by a partial removal of oxygen from the ITO layer and an associated increase of the electron concentration. While the reduction of Pb could be caused *chemically* by a removal of oxygen from the near interfacial region of the P(L)ZST, the rise of the Fermi energy, which could result in an *electrochemical* reduction of Pb (see Figure 1), is associated with a removal of oxygen from the ITO layer. The correlation between the Pb 4*f* binding energy and the reduction of Pb clearly reveals an upper limit of the binding energy of Pb, corresponding to an upper limit of the Fermi energy. For too high Fermi energies, the interface of P(L)ZST is not stable. The position of the Fermi energy at the interface is consequently a fundamental criterion for interface stability. For the case of dielectric oxides as those studied in this contribution, this directly affects the choice of metallic electrode materials suitable for co-sintering of multilayer ceramic capacitors.[5,25]

The Fermi energy in P(L)ZST can be quantified from the binding energy of the oxidic Pb 4*f* component relative to the valence band maximum. Such values have to be determined from the bare surfaces of a material.[26] For this purpose, we use a set of data available from room temperature measurements of bulk ceramic and thin film PZT samples with different compositions. The values obtained are $BE_{VB}^{Pb\,4f} = 136.5 \pm 0.2$eV and $BE_{VB}^{Zr\,3d} = 179.9 \pm 0.2$eV. As the energy gap varies with temperature, the Fermi energy is extracted from the spectra measured after cooling to room temperature without applied field. Thereby, it is revealed that the reduction of Pb occurs when the Fermi energy rises to 2.45 ± 0.2 eV above the valence band maximum. This is more than 1 eV below the conduction band minimum.[27] The energetic situation is illustrated in Figure 4.

A crucial ingredient of the operando analysis of Fermi energy limits and the associated interface stability by means of photoelectron spectroscopy employing an electrochemical cell is the top electrode. This has to fulfill several requirements:

1. It needs to be thin enough to allow detection of photoelectrons from the substrate;
2. The electrode needs to be conductive enough at the given thickness to prevent voltage drops induced by the current flowing through it. A high resistivity of the used electrolyte material is beneficial;
3. A homogeneous electrode thickness can avoid inhomogeneous current and field distributions across the sample surface;
4. The deposition of the electrode material onto the substrate should be non-reactive. In the case of oxide substrates, interface reactions can be avoided by using conducting oxide electrodes;[28]
5. The Fermi energy in the electrode material needs to vary with the applied potential across the electrochemical cell. Cathodic/anodic polarization should raise/lower the Fermi energy in the electrode and thereby change the Schottky barrier height;
6. The reduction or oxidation potential of the electrolyte should lie within the range of the variation of the Fermi energy of the electrode materials;
7. The electrode material should be stable under operation of the electrochemical cell.

Apparently, all conditions are fulfilled in the presented experiments, in which ITO has been used as cathode in a solid oxide electrochemical cell with P(L)ZST as electrolyte. The electrical conductivity of ITO can be as high as 10^4 Scm^{-1}, leading to sheet resistances <1 kΩ at a thickness of 4 nm. However, the undoped PZST sample has been too conductive, such that condition two is not fulfilled for higher fields. It is noted that condition two is

also not fulfilled if ITO is used as anode material. In this case, the ITO electrode is oxidized, resulting in a substantial reduction of its electrical conductivity due to incorporation of oxygen.

Future studies will involve different oxides as electrolyte materials and extend the approach to the anode side of the cells in order to reveal lower limits of the Fermi energy. Suitable anode materials are yet to be identified. A critical issue will be the stability of the anode material at elevated temperature, particularly in ultrahigh vacuum. It may become necessary to perform such studies in a near-ambient pressure system, in which photoelectron spectroscopy can be performed in more oxidizing environments.[29] Different challenges will arise for studying other "electrolyte" materials. Materials of interest may exhibit an electronic conductivity too high for applying electric fields high enough to induce ion migration. Too high currents will also lead to voltage drops along the electrode layer and related binding energy shifts. An alternative is then to use such materials as electrode with an ion conducting electrolyte, such as YSZ.[10–14] For chalcogenides, which can also exhibit low temperature field-induced ion migration,[30] suitable electrode materials need to be identified that fulfill the criteria listed above. With the use of high-energy XPS, thicker electrode materials can be applied, increasing the range of electrode materials and also allowing for higher conductive electrolyte materials. The application of the technique to thin film electrolytes can also be challenging. In the present experiment, contacts with >4 mm diameter were required, which may result in short circuits when applied to thin films.

3. Conclusion

Operando XPS analysis of solid oxide cells with highly-resistive antiferroelectric P(L)ZST and ITO as cathode demonstrated a correlation between the chemical reduction of the P(L)ZST and the Fermi energy at the interface. The experiments constitute a unique approach to access interface stability. Combined information on chemical and electronic interface properties provided by X-ray photoelectron spectroscopy can reveal not only the chemical reactions occurring during degradation but also electrochemical reduction mechanisms. The observations emphasize the importance of electrostatic boundary conditions and offer new insights into the degradation mechanism. As sample geometries close to real device configurations can be employed, the experiments will establish realistic scenarios for degradation mechanisms based on interface properties.

4. Experimental Section

The P(L)ZST bulk ceramics with a *B*-site composition of 75 % Zr, 16 % Sn, and 9 % Ti had been prepared using conventional solid-state ceramic route. The final sintering step was at 1250 °C for 3 h. The doped sample was located on the Ti-poor side of the phase boundary between ferroelectric and antiferroelectric regions in the 2 % La-doped PZST phase diagram,[31] and the undoped one keeps the same *B*-site ratio as the La-doped composition. Polarization hysteresis loops and temperature dependent permittivity were shown in Figure S1 (Supporting Information).

For the electrochemical cell (Figure 1c), the P(L)ZST samples were ground to a final thickness of 200 – 300 µm. Pt was used as bottom electrode with a thickness of 50 nm. As top electrode, 3 – 4 nm thick ITO films with 10 % Sn doping were applied. Before deposition, surface cleaning of the ceramic samples was carried out by heating in the deposition chamber in 0.5 Pa O_2 gas at 350 °C for 1 h to remove adventitious carbon.[32] The ITO films were then deposited by radio-frequency magnetron sputtering at a substrate temperature of 350 °C in pure argon atmosphere, resulting in an electrical conductivity of >5000 Scm^{-1}. According to our extensive experience with interface analysis, the ITO film was expected to cover the P(L)ZST substrates homogeneously, despite its low film thickness. One reason was the used magnetron sputtering technique that was known to induce a high density of nucleation sites.[33] The substrate cleaning would promote this effect. The homogeneous coverage was confirmed by an exponential decay of the substrate emissions with increasing film thickness and an attenuation length, which corresponds to the inelastic mean free path. In addition, polarization hysteresis loops measured inside the XPS system with the thin ITO electrodes were identical to those measured in silicone oil with thick electrodes (see Figure S1, Supporting Information). This would not be the case for inhomogeneous surface coverage.

The samples were mounted on a sample holder allowing electrical contacts to both electrodes. The top electrode was connected to ground, ensuring that the Fermi energy at the top of the sample was aligned with that of the spectrometer, which serves as binding energy reference for the spectra. The latter was calibrated by means of a sputter-cleaned Ag foil. The cell was positioned on a temperature controlled sample manipulator in the XPS system (PHI 5700, Physical Electronics, Chanhassen, USA) for monitoring the changes of the Fermi energy and chemical states by means of XPS. XP spectra were excited by monochromatic Al Kα radiation and recorded at a takeoff angle of 45 °. The current flowing through the sample with applied electric field had been monitored using a Keithley 6487 picoammeter (Tektronix, Inc., USA). The measurements are given in the Supporting Information.

Supporting Information

Supporting Information is available from the Wiley Online Library or from the author.

Acknowledgements

This work had been supported by the state of Hesse in the frame of the LOEWE research project FLAME (Fermi level engineering of antiferroelectric materials for energy storage and insulation systems).

Conflict of Interest

The authors declare no conflict of interest.

Data Availability Statement

The data that support the findings of this study are available from the corresponding author upon reasonable request.

Keywords

anti-ferroelectrics, electrochemical cells, interface stability, operando, X-ray photoelectron spectroscopy

Received: April 24, 2023
Revised: May 22, 2023
Published online:

[1] Y. Xiao, Y. Wang, S.-H. Bo, J. C. Kim, L. J. Miara, G. Ceder, *Nature Rev. Mater.* **2020**, *5*, 105.

[2] X. J. Lou, M. Zhang, S. A. T. Redfern, J. F. Scott, *Phys. Rev. Lett.* **2006**, *97*, 177601.
[3] D.-Y. Cho, M. Luebben, S. Wiefels, K.-S. Lee, I. Valov, *ACS Appl. Mater. Interfaces* **2017**, *9*, 19287.
[4] C. A. Randall, A. Kelnberger, G. Y. Yang, R. E. Eitel, T. R. Shrout, *J. Electroceram.* **2005**, *14*, 177.
[5] L. Gao, H. Guo, S. Zhang, C. A. Randall, *Actuators* **2016**, *5*, 8.
[6] P. Atkins, J. de Paula, J. Keeler, *Physical Chemistry*, 12 Ed., Oxford University Press, Oxford **2023**.
[7] A. Walsh, A. Zunger, *Nature Mater.* **2017**, *16*, 964.
[8] C. Lohaus, A. Klein, W. Jaegermann, *Nature Commun.* **2018**, *9*, 4309.
[9] C. A. Randall, Z. Fan, I. Reaney, L.-Q. Chen, S. Trolier-McKinstry, *J. Am. Ceram. Soc.* **2021**, *104*, 3775.
[10] A. Nenning, A. K. Opitz, C. Rameshan, R. Rameshan, R. Blume, M. Hävecker, A. Knop-Gericke, G. Rupprechter, B. Klötzer, J. Fleig, *J. Phys. Chem. C* **2016**, *120*, 1461.
[11] A. K. Opitz, A. Nenning, C. Rameshan, R. Rameshan, R. Blume, M. Hävecker, A. Knop-Gericke, G. Rupprechter, J. Fleig, B. Klötzer, *Angew. Chem.-Int. Edit.* **2015**, *54*, 2628.
[12] A. K. Opitz, C. Rameshan, M. Kubicek, G. M. Rupp, A. Nenning, T. Götsch, R. Blume, M. Hävecker, A. Knop-Gericke, G. Rupprechter, B. Klötzer, J. Fleig, *Topics in Catalysis* **2018**, *61*, 2129.
[13] Q. Lu, S. R. Bishop, D. Lee, S. Lee, H. Bluhm, H. L. Tuller, H. N. Lee, B. Yildiz, *Adv. Funct. Mater.* **2018**, *28*, 1803024.
[14] Q. Lu, G. Vardar, M. Jansen, S. R. Bishop, I. Waluyo, H. L. Tuller, B. Yildiz, *Chem. Mater.* **2018**, *30*, 2600.
[15] H. Kishi, Y. Mizuno, H. Chazono, *Jpn. J. Appl. Phys.* **2003**, *42*, 1.
[16] C. A. Randall, H. Ogihara, J. R. Kim, G. Y. Yang, C. S. Stringer, S. Trolier-McKinstry, M. Lanagan, in *Proc. of the 2009 IEEE Pulsed Power Conference*, Washington, DC **2009**, pp. 346–351.
[17] T. Baiatu, R. Waser, K.-H. Härdtl, *J. Am. Ceram. Soc.* **1990**, *73*, 1663.
[18] N. S. Bein, P. Machado, M. Coll, F. Chen, M. Makarovic, T. Rojac, A. Klein, *J. Phys. Chem. Lett.* **2019**, *10*, 7071.
[19] C. Körber, V. Krishnakumar, A. Klein, G. Panaccione, P. Torelli, A. Walsh, J. L. F. D. Silva, S.-H. Wei, R. G. Egdell, D. J. Payne, *Phys. Rev. B* **2010**, *81*, 165207.
[20] K. Irmscher, M. Naumann, M. Pietsch, Z. Galazka, R. Uecker, T. Schulz, R. Schewski, M. Albrecht, R. Fornari, *phys. stat. sol. (a)* **2014**, *211*, 54.
[21] B. Akkopru-Akgun, T. J. M. Bayer, K. Tsuji, K. Wang, C. A. Randall, M. T. Lanagan, S. Trolier-McKinstry, *J. Appl. Phys.* **2021**, *129*, 174102.
[22] D. R. Lide, editor, *CRC Handbook of Chemistry and Physics*, 85 Ed., CRC Press, Boca Raton **2005**.
[23] D. M. Smyth, *The defect chemistry of metal oxides*, Oxford University Press, Oxford **2000**.
[24] R. Schafranek, S. Li, F. Chen, W. Wu, A. Klein, *Phys. Rev. B* **2011**, *84*, 045317.
[25] K. Hong, T. H. Lee, J. M. Suh, S.-H. Yoon, H. W. Jang, *J. Mater. Chem. C* **2019**, *7*, 9782.
[26] S. A. Chambers, T. Droubay, T. C. Kaspar, M. Gutowski, M. van Schilfgaarde, *Surf. Sci.* **2004**, *554*, 81.
[27] H. Lee, Y. S. Kang, S.-J. Cho, B. Xiao, H. Morkoç, T. D. Kang, G. S. Lee, J. Li, S.-H. Wei, P. G. Snyder, J. T. Evans, *J. Appl. Phys.* **2005**, *98*, 094108.
[28] A. Klein, *J. Am. Ceram. Soc.* **2016**, *99*, 369.
[29] M. Salmeron, R. Schlögl, *Surf. Sci. Rep.* **2008**, *63*, 169.
[30] K. Gartsman, L. Chernyak, V. Lyahovitskaya, D. Cahen, V. Didik, V. Kozlovsky, R. Malkovich, E. Skoryatina, V. Usacheva, *J. Appl. Phys.* **1997**, *82*, 4282.
[31] D. Berlincourt, *IEEE Transactions on Sonics and Ultrasonics* **1966**, *13*, 116.
[32] Y. Gassenbauer, R. Schafranek, A. Klein, S. Zafeiratos, M. Hävecker, A. Knop-Gericke, R. Schlögl, *Phys. Rev. B* **2006**, *73*, 245312.
[33] M. Ohring, *The Materials Science of Thin Films*, Academic Press, San Diego **1992**.